A DEFT way to forecast solar flares

Larisza D. Krista[1, 2, 3] and Matthew Chih[4]

[1]*Cooperative Institute for Research in Environmental Sciences, University of Colorado, Boulder, CO 80309, USA*
[2]*National Centers for Environmental Information, National Oceanic and Atmospheric Administration, Boulder, CO 80305, USA*
[3]*Space Science Institute, Boulder, CO 80301, USA*
[4]*Marietta College, Marietta, OH 45750, USA*

ABSTRACT

Solar flares have been linked to some of the most significant space weather hazards at Earth. These hazards, including radio blackouts and energetic particle events, can start just minutes after the flare onset. Therefore, it is of great importance to identify and predict flare events. In this paper we introduce the Detection and EUV Flare Tracking (DEFT) tool, which allows us to identify flare signatures and their precursors using high spatial and temporal resolution extreme-ultraviolet (EUV) solar observations. The unique advantage of DEFT is its ability to identify small but significant EUV intensity changes that may lead to solar eruptions. Furthermore, the tool can identify the location of the disturbances and distinguish events occurring at the same time in multiple locations. The algorithm analyzes high temporal cadence observations obtained from the Solar Ultraviolet Imager (SUVI) instrument aboard the GOES-R satellite. In a study of 61 flares of various magnitudes observed in 2017, the "main" EUV flare signatures (those closest in time to the X-ray start time) were identified on average 6 minutes early. The "precursor" EUV signatures (second-closest EUV signatures to the X-ray start time) appeared on average 14 minutes early. Our next goal is to develop an operational version of DEFT and to simulate and test its real-time use. A fully operational DEFT has the potential to significantly improve space weather forecast times.

Keywords: Sun: corona — Sun: solar flares — Techniques: image processing

1. INTRODUCTION

It is well known that significant extreme-ultraviolet (EUV) and X-ray radiation occurs at the time of a flare. This radiation can be observed at the flare footpoints where plasma is heated by non-thermal electron beams. The electrons are accelerated through magnetic reconnection and some of them travel down along the magnetic field lines and bombard deeper layers of the atmosphere. (Brown 1971). Mrozek et al. (2007) showed that higher energy electrons are able to pass deeper into the atmosphere and lead to EUV radiation at the flare footpoints. Studying the October 28, 2003 X17 class flare Su et al. (2006) found magnetic shear in the flare region that decreased significantly during the impulsive phase of the flare. They also found EUV brightenings before the hard X-ray emission, that appeared to be associated with the main-phase flare. Su et al. (2006) hypothesized that the EUV brightenings that occurred before the X-ray emission have the same generation mechanism as the ones that appeared during the flare. In this paper we present evidence that with a highly sensitive instrument and the right processing tools, pre-flare EUV signatures can be detected for all magnitudes of flares and potentially used for space weather forecasting.

Understanding the physical processes leading to solar flares and developing tools to identify them early is essential for space weather forecasting. Solar flares can cause a number of space weather hazards at Earth: the X-ray radiation from flares increases the ionization of the ionosphere (Tobiska et al. 2000), potentially leading to high frequency radio blackouts; and the energetic particles from flares can disrupt technological systems and human activities in space. Furthermore, since the radiation originating in the flares travels at the speed of light, the impacts are often felt by the time the flares are detected.

Over the last decade, there have been many advancements in flare forecasting. A large number of prediction tools now utilize machine learning (ML) methods (e.g. support vector machine, k-nearest neighbors, randomized trees,

random forest) in order to forecast the likelihood of flares occurring in the next 24 hours (Nishizuka et al. 2021; Asaly et al. 2021; Abed et al. 2021; Panos & Kleint 2020; Li et al. 2020; Deshmukh et al. 2020; Wang et al. 2020; Jiao et al. 2020; Tlatov et al. 2020; Domijan et al. 2019; Liu et al. 2019; Alipour et al. 2019; Chen et al. 2019; Zheng et al. 2019). Many of these methods claim to have relatively high skills scores for forecasting flares. However, these evaluations can be dependent on the database used and the type of performance metrics chosen. Leka et al. (2019) analyzed a large number of forecast methods and the results showed that while many methods performed above the "no skill" level, none of the operational flare forecasting methods performed above 0.5 across all evaluation metrics. Note, 0.5 is the value halfway between "no skill" and "perfect".

Furthermore, ML methods can be computationally heavy, can require multiple data inputs that might not be readily available real-time and their success is dependent on the initial training dataset. For this reason, most of them are not ready for operational, real-time space weather forecasting. While there is undoubtedly value in forecasting the possibility of a flare within 24 hours (a capability offered by numerous ML methods), in the realm of operational space weather preparedness, there is even more value in forecasting an impending flare within an hour. A shorter, more precise lead-time can give industries and agencies vulnerable to space weather disturbances a chance to minimize interruption to services and operations.

Among the flare prediction tools that do not use ML, Shramko et al. (2019) demonstrated the possibility of forecasting flares within 24 hours relying solely on microwave radiation signatures. Goodman et al. (2020) studied 14 active regions and showed that increases in the photospheric resistive heating rate in active regions are correlated with the occurrence of M and X flares a few hours to a few days later. Morales & Santos (2020) investigated the predicting capabilities of the Lu and Hamilton self-organised-criticality avalanche model (Lu & Hamilton 1991). In the cases studied, they found that in more than half of the cases there was enough information to predict large or extreme events.

Flare forecast methods are often difficult to compare because they analyze different datasets. Barnes et al. (2016) reviewed and systematically compared eleven statistical forecast methods that rely on photospheric magnetic field and continuum intensity observations (for more details on the methods, see Barnes et al. (2016)). The comparative study showed that none of the methods stood out or achieved high skill score values.

Guerra et al. (2020) investigated ensemble forecasting for major solar flares by linearly combining full-disk probabilistic forecasts from six operational forecasting methods. 28 ensembles were created to study M and X-class flare forecasts. They found that the majority of ensembles not only performed better than the ensemble members alone, but also better than the equal-weights ensemble. While this is a promising result, an ensemble forecasting method would be more computationally heavy and require more time to provide a forecast, compared to just one model. Such an ensemble might also rely on data that is not readily available real-time.

It is clear that the challenge to construct a real-time, consistent and robust flare forecasting method is still ongoing. It is also important to emphasize that any competitive forecast method needs to rely primarily on data that is acquired near-real time - without this, even the best forecasting tool will fall short of operational use.

In order to mitigate the impacts of flare-related space weather events, it is critical to identify flares as early as possible. Ideally, we would not only identify flares as they happen, but predict them in advance. However, the latter is still a major challenge. This lack of predictive capability indicates that we have yet much to discover about the physics of flares: how flares are initiated; whether there are different processes that trigger flares; the potential differences between flare initiation mechanisms; when these mechanisms start and when/if they are observable by currently available instruments; whether the magnetic configuration of an active region is a key factor in the initiation, recurrence and magnitude of flares. These are questions that have been extensively studied and yet are still highly debated in the solar physics community. As of this moment, consistent and reliable flare prediction is still out of reach.

Flares have been, and are still primarily detected using space-based instruments measuring solar X-ray irradiance (e.g. the XRS instrument aboard the GOES spacecraft; Hanser & Sellers, 1996). However, these measurements suffer from several important limitations, which also affect the globally trusted flare detection methods used by the National Oceanic and Atmospheric Administration Space Weather Prediction Center (NOAA/SWPC). Firstly, since X-ray irradiance is an integrated signal, the location of the source region is unknown (it is identified manually after the fact). Furthermore, using irradiance we cannot know whether the signal came from one or more regions and how the distribution of the signal changed over time. Secondly, in order to avoid false detections due to small variations in the coronal background, SWPC's detection method requires a rise in the total X-ray irradiance for at least four consecutive minutes and a total increase of at least 40% before it registers a flare (Ryan et al. 2016). Hence, there is

an inherent delay in this flare detection method. Also, XRS is not sensitive enough to identify weak flare precursor signatures that might be evident in solar imagery but not in the total X-ray irradiance of the Sun.

As mentioned above, this approach is also limited when co-temporal flares occur: a second flare can be detected—only after the irradiance drops below 50% of the difference between the pre-flare flux and the peak flare flux. This means that the method sometimes fails to appropriately identify flares that occur at or around the same time in different locations on the Sun. Typical forecasting scenarios only allow for alerts, issued when flare irradiance reaches a certain threshold, and follow-up summary messages are generally issued well after the peak of a flare event. At SWPC, alerts are issued when irradiance reaches the M5 level flare threshold, with no pre-alert warning.

We propose to complement and improve on current operational flare detection strategies using state-of-the-art, real-time, low-latency observations from the Solar Ultraviolet Imager (SUVI, Tadikonda et al., 2019; Fulbright et al., 2017) instrument aboard the GOES-R satellite. Preliminary tests of our new detection method – the Detection and EUV Flare Tracking, aka DEFT – reveal improvements of several minutes in main-phase flare alert times, and over ten minutes in precursor signature detection. Furthermore, we can also detect and separately track concurrent events. These improvements can yield important gains in prediction times for solar flares and they could allow warnings to be issued in advance of the primary onset of a major flare – which is currently not possible. In the following sections we will describe the data we used (Section 2); our new detection method (Section 3) and the initial results of our investigation (Section 4). We conclude by discussing the implications of DEFT for the future of **flare warning** and space weather forecasting and how we will further develop our tool (Section 5).

2. INSTRUMENT AND OBSERVATIONS

SUVI is a normal-incidence extreme-ultraviolet (EUV) Ritchey-Chrétien telescope that observes the solar atmosphere in six ultraviolet passbands — 93, 131, 171, 195, 284, and 304 Å — corresponding to emission from ion species at a range of temperatures between about 50,000 K and 20 MK. SUVI images are approximately 53.3 × 53.3 arcmin, 1280 × 1280 pixel square images with a plate scale of 2.5 arcsec. Each SUVI instrument operates at a cadence of 10 s, obtaining images at a variety of wavelengths and exposure times. SUVI observations extend back to early 2017 (at this moment, public data is only available from May 2018).

Narrowband images, such as those we use from SUVI are capable of distinguishing plasma at a wide range of temperatures, and they are sensitive to a variety of possible signs of flare onset that can occur before the production of high-temperature plasma (generally observed in X-rays). Because different passbands correspond to ion species at different temperatures, various narrowband image channels respond differently to flares depending on when and where heating or cooling of the flare-associated plasma is occurring. The overall sensitivity of the EUV images we use allow us to detect very small, localized changes in radiance that would not be detectable in integrated flux measurements. Furthermore, SUVI observations provide imaging (as opposed to integrated signal), which allows us to resolve the locations of flares and their temporal changes. Thus, we are able to distinguish events that are happening at or around the same time, which is impossible with irradiance observations.

On global scales EUV emission tends to brighten some time after more energetic emissions like X-rays. However, smaller features typically brighten at or before the onset of eruptions, particularly in high-temperature channels where plasma might be energized by the initial onset of magnetic reconnection. Reeves & Golub (2011) and Savage et al. (2012) discuss such a case, where structures that are clearly associated with reconnection in a current sheet were the earliest signs of an eruptive flare. These bright structures are relatively small, so they do not significantly influence the total solar irradiance early in the flare and might not be detectable in irradiance measurements. However, they could be detectable in EUV images.

3. THE DEFT FLARE DETECTION METHOD

Our goal with DEFT is to identify solar flares of space weather relevance in EUV observations quickly, consistently and with minimal computational overhead. We assembled a catalogue of 61 flares from 2017, using GOES-R 16/SUVI data. We stored their magnitude and X-ray start-time using the SWPC flare database. We then obtained GOES/SUVI EUV observations before and after the recorded flare start times. This was done in order to identify possible EUV signatures before the flare X-ray start time or afterwards, if none was identified beforehand.

We investigated the efficiency of the six available SUVI wavelengths at detecting pre-flare EUV signatures. The temporal cadence for some wavelengths is not optimal: the 131, 171 and 284 Å wavelength observations have a cadence of 4 minutes which could mean a 4 minute delay in detection. The 94 Å wavelength observations have higher

cadence (2 minutes), but they are best for observing the main stage flare (multi-million Kelvin corona signatures). For the 94 Å wavelength the signature comes after the X-ray start time, so it is not very useful for forecasting. The 195 Å wavelength has a higher cadence (1 minute) but detects a lot of intensity fluctuations and is also better for observing the main stage flare (after the X-ray start time). The 304 Å wavelength observations are higher cadence (2 minutes), and they capture pre-flare signatures in the transition region/chromosphere (<100.000 K). For this reason the current version of DEFT only relies on the 304 Å wavelength.

From this point on the analysis is fully automated: the DEFT algorithm first creates a mask to analyze a disk in the observation. This mask is centered on, and is slightly larger than the solar disk. The mask allows us to exclude any erroneous signatures that could occur off-disk, but include flare signatures that occur on-disk, or even slightly above the limb. Next, an intensity histogram is created using the observed disk. The histogram helps distinguish high intensity flare and pre-flare signatures from the rest of the disk. We store the resulting full-disk and sub-image of the possible flare signature site, as well as the physical properties of the signature: heliographic location, EUV intensity peak, pixel count, and the corresponding running difference values.

High intensity signatures can also appear at the same time, in different locations. For this reason we developed a spatial discriminator that groups together high-intensity pixels based on their spatial proximity (within 10 degrees only, to avoid other regions) and help distinguish separate regions of activity. This means that we can analyze separate regions and determine which ones display pre-flare activity and which ones do not. The signal in a group is summed and treated as one source. Once the signature groups are created, DEFT can determine if any group has trespassed the threshold and it can flag possible pre-flare activity. DEFT also determines the location of the activity - a key factor in understanding and providing alerts for flares that could pose a real risk of space weather hazards such as radio blackouts, and risks to GPS navigation, EVAs and satellite operations.

Figure 1 shows an observation where two high intensity EUV sources were identified: AR 12673 near the west limb (highlighted in red in the left panels), and AR 12677 in the eastern hemisphere (highlighted in red in the right panels). A third region – AR 12674 – is visible in the NW quadrant, but this region did not contain pixels with high enough intensity, and hence, we do not discuss it. The high intensity pixels were located, grouped together based on their proximity and labelled as two separate sources. This process is essential to accurately determine the EUV intensity at any given time and to track temporal changes in each location separately. The image was taken with the GOES/SUVI instrument on 2017 Sep 7 at 9:45 UTC. In the top panels we show the same observation, but highlight each region of interest separately with red pixels and block out the other region (black) for processing and easier visual discrimination. In the panels right below, we show a zoomed-in image of the corresponding regions of interest. The panels on the left show the pre-flare EUV signal source which was linked to an M1.4 flare in AR 12673, with an X-ray start time of 9:49 UTC on 2017 Sep 7.

Once the EUV observations were processed with DEFT, we identified the signatures that appeared right before the flares. Using the start-time from the SWPC flare catalogue, the last two EUV signatures at or before the X-ray start time were identified and recorded. If no EUV signature at all was observed within an hour before the flare, the first signature after the X-ray start time was recorded. We refer to the signature closest to the X-ray start time as the "main signature" and the signature observed even earlier as the "precursor signature".

Once the pre-flare EUV signatures were identified for each of the 61 flares in our catalogue, their properties were statistically analyzed. Our goal is to better understand the EUV signatures that happen right before the X-ray flare: how/if the EUV signature properties are linked to flare magnitude, what their characteristics are, how early they occur, and whether they could be used for early space weather warnings. Identifying relationships between the X-ray flare properties and the EUV signatures could be used to develop DEFT into a real-time operational tool that could improve and/or complement the currently used X-ray based forecasting system at SWPC. Detecting the start of a flare even a few minutes early would be significant in itself since it would allow space weather alerts to be issued earlier than it has been possible until now. We found that there is a clear indication that pre-flare EUV signatures are detectable for B, C, M and X class flares several minutes early before the X-ray start time. In the following section we detail the statistical results of the DEFT detections.

4. RESULTS

The SUVI instrument provides observations in six different wavelengths, however, in the current work we only used the 304 Åwavelength that proved to be the most sensitive and successful in identifying both precursors and main stage events. Using the 2017 GOES X-ray flare catalogue we selected 61 flares: 4 X-class (the only X-class flares in 2017),
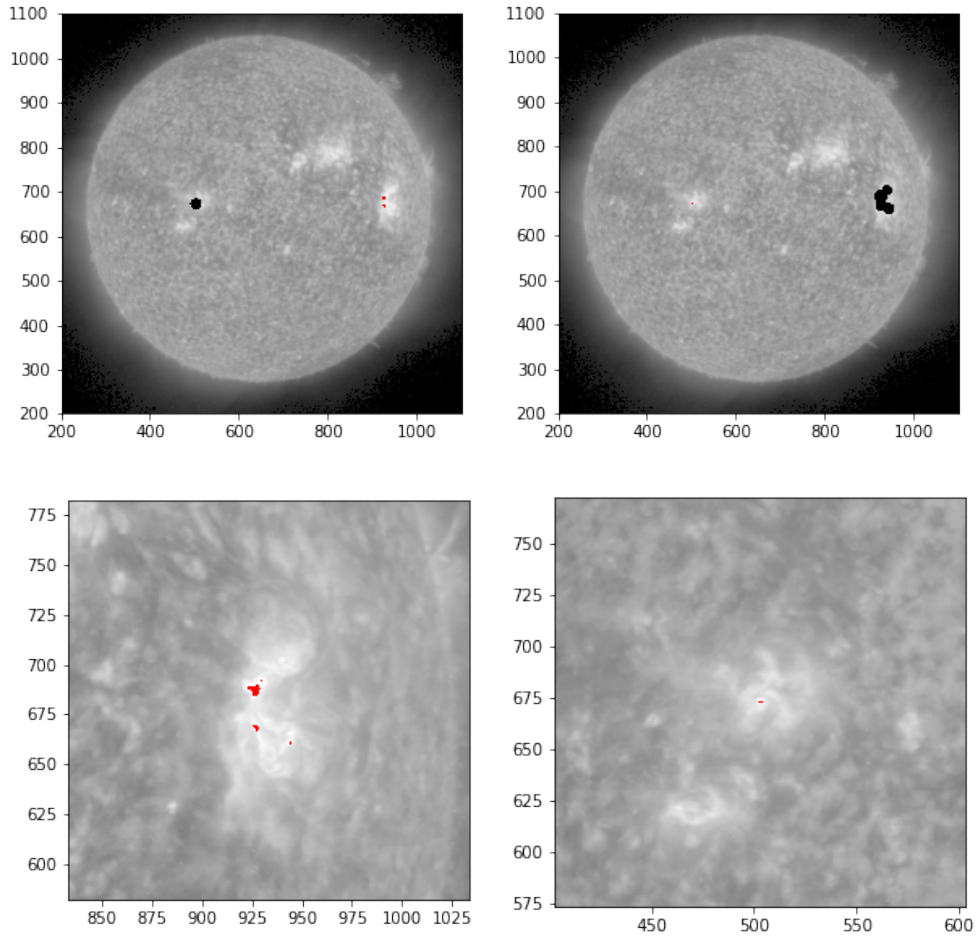
Figure 1. The spatial discrimination process of DEFT allows the accurate measurement and tracking of EUV signals originating in different regions. Both images show the same observation taken at the 304 Å wavelength with GOES-R/SUVI on 2017 Sep 7 at 9:45 UTC. Each image highlights one source in red, the other source is blocked out with black. The panel below each full-disk image shows a close-up of the corresponding region of interest (left panels highlight AR 12673 in red, the right panels highlight AR 12677). A pre-flare signal was identified in AR 12673 (see left panels), and was linked to an M1.4 flare that started at 9:49 UTC.

19 M-class, 19 C-class and 19 B-class flares. For every flare in the catalogue a "main" EUV signature was identified. However, for one X and one M class flare (both limb flares), and for 2 C and 8 B flares no "precursor" EUV signature was found. And aside from the 61 flares discussed in this paper, we also found 3 small flares with no EUV signatures at all (a B1, B2, and a B3 flare).

The main and precursor signatures were analyzed separately for each flare class. The panels from left to right in Figure 2 show the time difference (Δt), total pixel count and pixel count change averaged for each class. Δt signifies the time between the EUV pre-flare signal and the official start of the X-ray flare. Total pixel count refers to the total number of EUV pre-flare signature pixels. The pixel rate of change is the change in the signature pixel numbers at the time when the EUV pre-flare signal was detected. Blue corresponds to the precursor signal (the second to last signal before the official X-ray start time) and red corresponds to the main EUV signal (the last signal before the official X-ray start time). The typical mean Δt values for EUV precursors were 17, 16, 11 and 12 minutes for B, C, M and X class flares, respectively. The typical mean Δt values for the main EUV signals were 6, 8, 2 and 9 minutes early for B, C, M and X class flares, respectively.

We emphasize that these times are compared to the X-ray start time. Compared to the NOAA/SWPC alerts we gain an additional 4 minutes at least. This means that apart from the M class main signatures, across all classes we recorded EUV signature times that were over 10 minutes earlier than the earliest SWPC alert times. Also, the middle

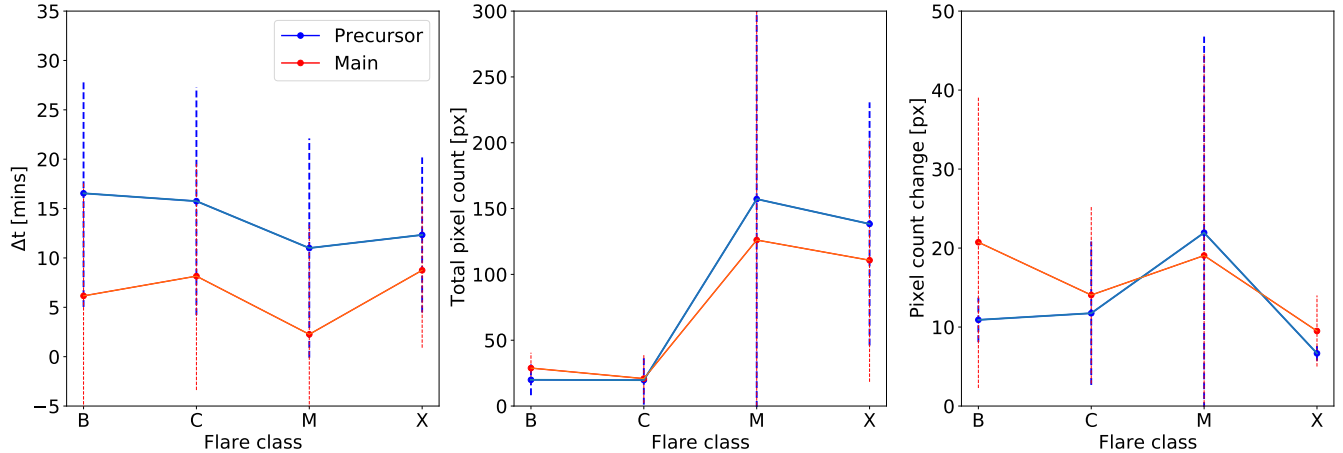**Figure 2.** From left to right: the mean Δt, total pixel count, and the pixel count change for each flare class. Blue and red correspond to precursor and main signature properties, respectively. (Δt is the time difference between the EUV signal and the flare X-ray start time. Total pixel count is the total number of pixels in the EUV flare signature. The pixel count change is the change in the flare pixel numbers when the EUV pre-flare signal was identified.)

panel shows that M and X class flares were observed to have significantly higher pixel count rates on average. This result will be useful in developing DEFT's ability to estimate flare magnitudes.

The top row in Figure 3 shows density scatter plots for the main signal properties (darker color indicates higher density). From left to right the density scatter plots show Δt, total pixel count, and the pixel count change. The lower panels show the same values from left to right for precursor signatures. The Spearman (S) correlation values are shown in each panel. The highest correlation is between the flare magnitude and the pixel count for both precursor and main signatures (middle panels in Figure 3): the Spearman correlation coefficient is 0.39 (p-value = 0.0017) and 0.5 (p-value = 0.0003), respectively. This indicates a moderate positive monotonic relationship between flare magnitude and the EUV signature pixel count. We also highlighted the location of flux equivalent of an M1 flare (vertical red line in the middle panels). More than 90% of the data points for pixel count were under 100 counts. Note that pixel counts over 100 (shown with a horizontal red line) only occur for M and X-class flares – both for main and precursor signals.

Note that a p-value of less than 0.05 suggests a statistically significant correlation, and our values were considerably lower. No other significant correlation was found between the flare magnitudes and the EUV properties listed. We also calculated the Pearson correlation values, but these were very low and not statistically significant.

We also analyzed the relationship between main and precursor signal properties (Figure 4). The left panel of Figure 4 shows that the Δt values of main and precursor signals have a moderate Pearson (P = 0.49) and strong Spearman (S = 0.64) correlation with p-values well below 0.001. This indicates that earlier precursor signals could be accompanied by earlier main signals. We found strong correlation between the main and precursor pixel count values (middle panel of Figure 4): the Pearson and Spearman correlation coefficients were 0.93 and 0.68, respectively. The p-values were significantly below 0.001 for both. This suggests that larger precursor pixel counts tend to be accompanied by larger main signal pixel counts. No correlation was found between the pixel count change values (right panel of Figure 4).

Figure 5 shows histograms of the Δt values (left panels), the pixel count values (middle panels), and the pixel change values (right panels). The top row shows values for all flare magnitudes (B, C, M and X), the middle row shows values for only M and X class flares (the most important flares for space weather forecasting), the bottom panel shows values for the B and C flares only (these have low or no space weather impact). The histogram for the precursor values is shown in orange, the main signal values are shown in blue. The mean, mode and standard deviation values for the main and precursor signatures are listed under the corresponding labels.

Across all magnitudes, we could identify precursors on average 14 minutes, and main flare signatures 6 minutes earlier than the X-ray flare start time. For M and X flares combined this value was lower: 11 and 3 minutes, respectively. For B and C flares this value was considerably higher: 16 and 7 minutes, respectively.

The total pixel count of EUV signatures across all flare magnitudes was on average 79 for precursors and 62 for the main signal. This value was significantly higher for M and X flares combined: 155 pixels for precursors and 123 for
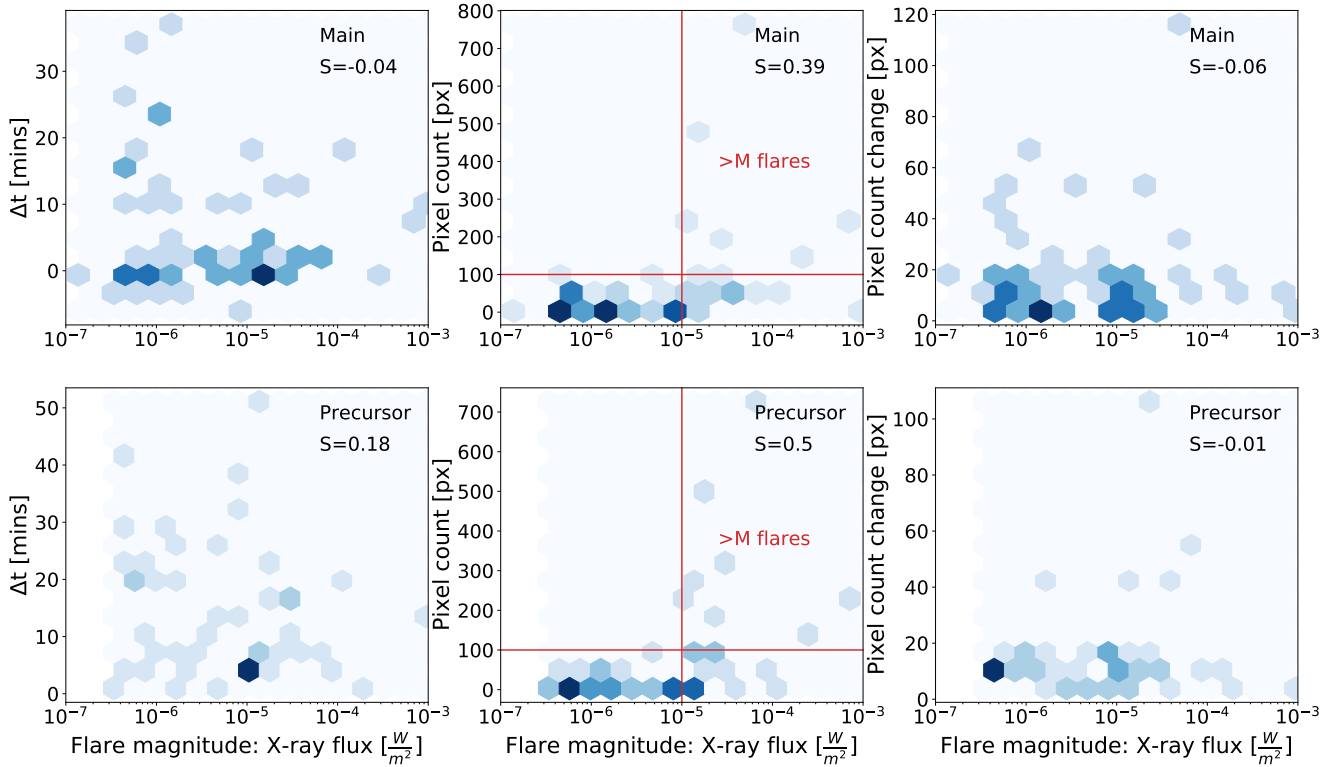
Figure 3. The upper and lower rows show main and precursor signal properties, respectively. From left to right the density scatter plots show Δt, the total pixel count, and the pixel count change for the EUV signals relative to flare magnitude. The Spearman (S) correlation values are listed in each panel. The vertical red line shows the flux that corresponds to an M1 flare, the higher values correspond to higher M and X-class flares. The horizontal red line denotes the 100 pixel count. (Note: fluxes of 10^{-7}, 10^{-6}, 10^{-5} and 10^{-4} W/m^2 correspond to B1, C1, M1, X1 flares, respectively.)
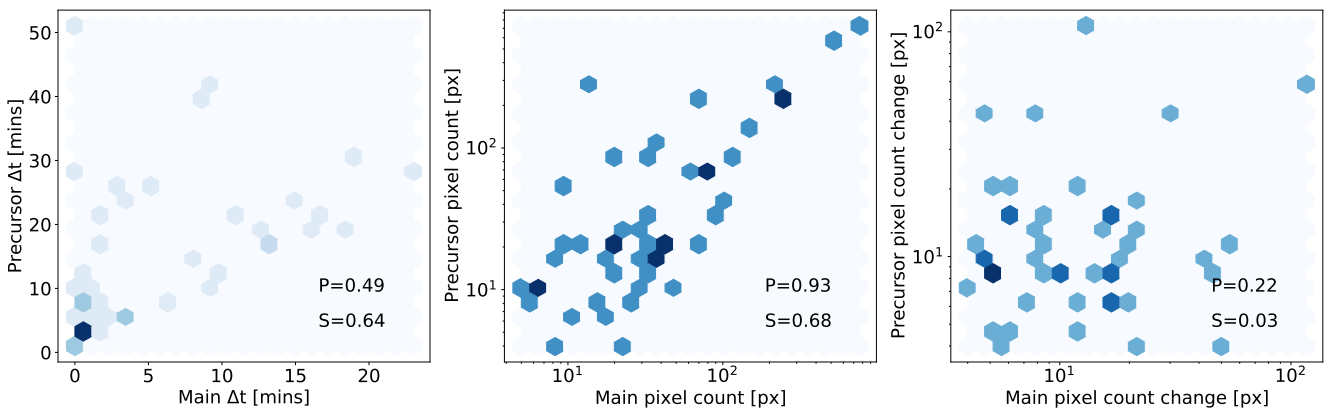
Figure 4. Density scatter plots showing the main and precursors signal properties relative to each other. The Pearson (P) and Spearman (S) correlation values are listed in each panel.

main signatures. For B and C flares this value was significantly lower: 20 for precursors and 25 pixels for the main signature.
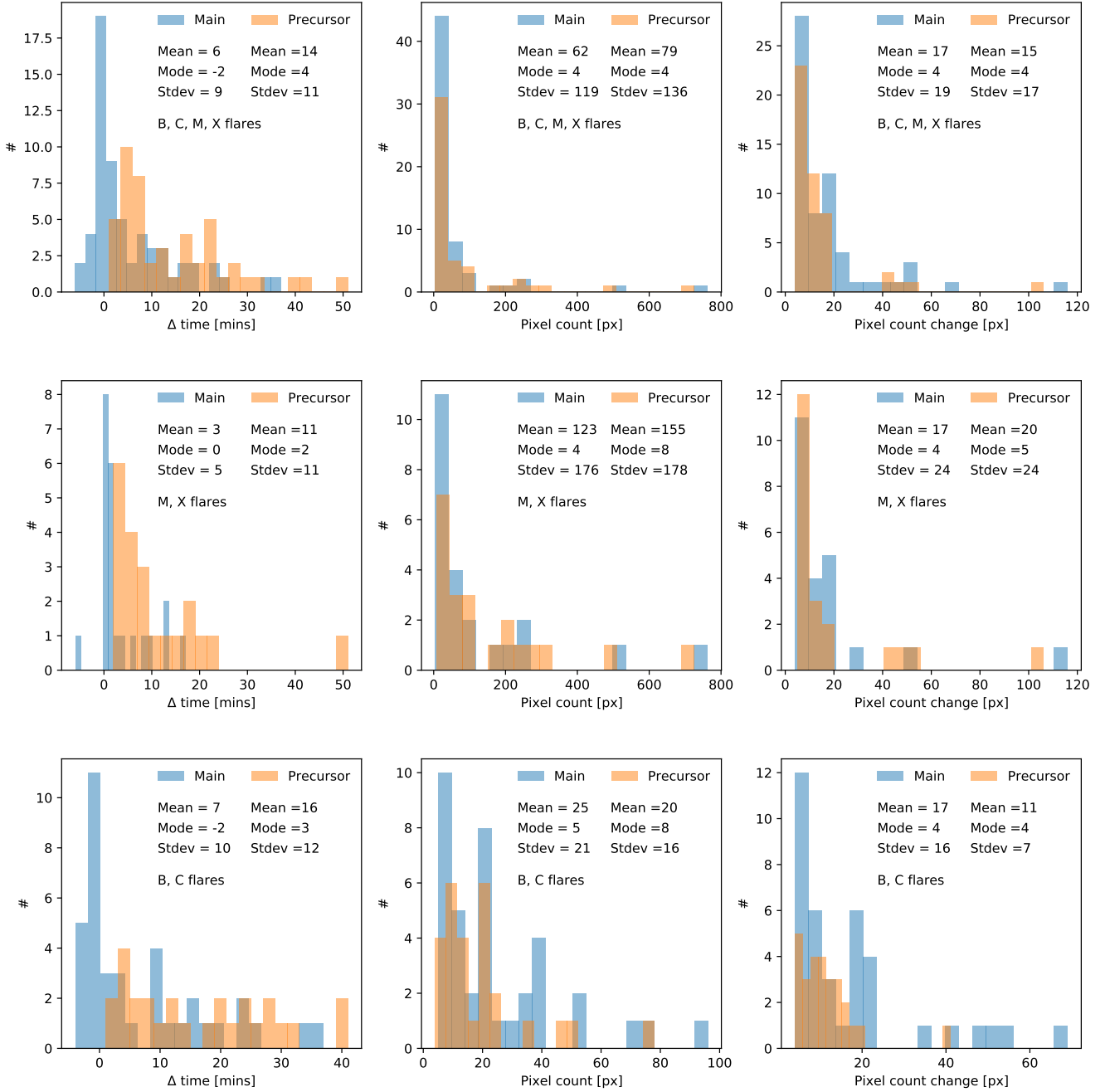
Figure 5. Histograms showing the Δt values (left panels), the pixel count values (middle panels), and the pixel count change values (right panels). The top row shows values corresponding to all flare magnitudes (B, C, M and X), the middle row shows values for only M and X class flares, the bottom panel shows values for the B and C flares only. The main signature values are shown in blue, the precursor histograms are shown in orange colour. The mean, mode and standard deviation values for the main and precursor signatures are listed under the corresponding labels.

Across all magnitudes the average pixel count change was 15 and 17 pixels for precursors and main signals, respectively. These values were a little higher for the high magnitude flares: 20 and 17 pixels, respectively. For low magnitude flares these values were somewhat lower: 11 and 17 pixels, respectively.

This shows that while M and X flares could be identified a little later than B and C flares, they can have significantly higher pixel counts than B and C class flares. Considering pixel count change values: larger flares demonstrate only slightly higher values.

When assembling our catalogue we had to exclude 7 B flares and 3 C flares that transitioned behind the limb, since we weren't able to identify any signatures. However, in 2 cases (an M and an X class flare) we could observe the main-stage flare despite the fact that the active region was mostly behind the limb (these cases are in our catalogue). For one flare DEFT identified no signal in the hour before the flare, the only signal identified was 6 minutes after the X-ray start-time. This was an M class flare at the solar limb that started on October 10, 2017 at 23:10 UTC, and was identified by DEFT at 23:16 UTC using existing data. Records show that SWPC identified it as a flare at 23:35 UTC (25 minutes after the X-ray start time), and the alert was issued at 00:27 UTC the next day (77 minutes after the X-ray start time). Hence, the identification time by DEFT was still at least 19 minutes earlier than the first recorded SWPC identification time.

The above mentioned cases suggests that the main-stage EUV signatures of higher magnitude (M and X) flares might still be observable by DEFT if the active region is at or slightly behind the observable limb, but we lose their precursor signatures and also most of the smaller (B and C) flare signatures. We plan to investigate specifically limb flares to better understand DEFT's limitations at the limb. Nevertheless, our analysis indicates that detecting the EUV flare signatures becomes more challenging at the solar limb.

5. CONCLUSIONS

Detection of pre-flare EUV signatures have the potential to not only improve space weather forecasting but also help us better understand the physical mechanisms leading to a flare. Mrozek et al. (2007) showed that higher energy electrons are able to penetrate deeper into the atmosphere (i.e. chromosphere). This finding is in alignment with the fact that the 304 Å observations, which are optimal for imaging the chromosphere, were the best for identifying pre-flare brightenings using DEFT. Furthermore, since the flare-related EUV radiation occurs near the flare footpoints, it could explain why the pre-flare EUV signals were harder to detect near the limb using DEFT. The closer a flare footpoints are to the limb the more the EUV signal decreases due to line-of-sight obscuration.

Su et al. (2006) analyzed the X17 flare of October 28, 2003 in EUV and hard X-ray observations. They found magnetic shear in the flare region that decreased significantly during the impulsive phase of the flare. They also found EUV brightenings before the hard X-ray emission, that appeared to be associated with the flare EUV brightenings. Su et al. (2006) hypothesized that the EUV brightenings that occurred before the X-ray emission were generated through the same mechanism as the brightenings that appeared during the flare. Our observations show that these pre-flare EUV brightenings are common - we observed them in all the flares in our study. They can be detected for flares of all magnitudes, which suggests that there is a similar process at work regardless of the magnitude of the flare. It is unclear why the signatures appear earlier for B and C flares and closer to the main phase for M and X flares. We found that small (B and C) flares have smaller EUV signatures (less than 100 pixel counts), while larger (M and X) flares can have both small and larger EUV signatures (up to 800 pixels). This means that a larger pre-flare EUV signature could indicate a larger instability in a region, and therefore could help us **estimate** the magnitude of a flare. We hypothesize that the pre-flare EUV brightenings are caused by micro-reconnections that temporarily relieve some of the instability in the region until the region reaches critical instability and erupts. In order to better understand the processes leading to a flare, further case studies are needed to investigate the evolution of the intensity of pre-flare EUV brightenings and their location relative to the magnetic inversion line and the main-phase EUV flare signal.

In this paper we introduced a novel approach to identify pre-flare EUV signatures within the hour before the X-ray start time. DEFT can identify pre-flare EUV intensity spikes in just a few pixels. It is a fast and robust tool that can locate a pre-flare signature on the solar disk within seconds. This is also possible because DEFT uses state-of-the-art data: high temporal and spatial cadence full-disk EUV observations from the GOES/SUVI instrument that are available near real-time and are not affected by saturation.

Many recently published ML flare forecasting methods only offer a binary prediction 24 hours ahead (e.g. Abed et al. (2021); Asaly et al. (2021); Li et al. (2020); Deshmukh et al. (2020); Park et al. (2018); Huang et al. (2018)), with a considerable false detection margin. Alerts 24 hours ahead are certainly beneficial, but limit the scope of mitigation: many instruments and infrastructures cannot be shut down for a whole day in preparation for a flare. Some forecast centers provide percentage chance flare forecasts, but still heavily rely on now-casting (i.e. identifying the flare as it happens and alerting after the event has already begun.) Now-casting is often too late to mitigate the effects of

flare-related high-energy particles impacting sensitive instruments or astronauts in EVA. Our aim is to develop a tool that provides alerts early enough for space weather mitigation purposes, while also minimising the time needed to put instruments into safe-mode before the impact of high-energy particles related to flares.

In particular, we want to improve space weather alert times by identifying and understanding EUV signatures before flares occur, and developing a tool to consistently detect them. In our study we identified the last two EUV signatures before 61 flares of various magnitudes. We consistently identified a "main" EUV signal on average 6 minutes, and a "precursor" EUV signal on average 14 minutes before the X-ray start time. We also found that when separating M and X class flares from B and C class flares (based on the severity of their potential space weather impact), the higher class flares could have significantly higher pixel count values. This result could help us develop a way to **estimate** flare magnitudes in the future. Furthermore, we found that higher precursor pixels counts are positively correlated with higher main signal pixel counts, which means that the precursor could help us determine the expected magnitude even earlier. By studying flares close to the limb we learned about the limitations of DEFT: EUV signals occurring close to the limb have less lead-time compared to the X-ray start time. This is likely due to line-of sight observational limitations in EUV.

Our study shed light on the properties of pre-flare EUV signals, their relationship with flares and the possible mechanisms causing them. The results will help us to adapt the DEFT algorithm into an operational tool. The next stage of our project involves adapting DEFT to run on a large blind database, identifying pre-flare EUV signatures, filtering out false positives and making sure all large flares are detected. This process essentially simulates operational use. We are currently working on an updated DEFT, and initial tests show that it is successful in identifying all major flares in blind data, while also eliminating almost all false positives. **In our next publication, we will detail the operational version of DEFT and the results of a large statistical blind study. In addition we will also test DEFT on other EUV datasets (e.g. SDO/AIA)**. Our ultimate goal is to run DEFT on real-time GOES/SUVI data and improve flare forecast times.

6. ACKNOWLEDGMENTS

REFERENCES

Abed, A. K., Qahwaji, R., & Abed, A. 2021, Advances in Space Research, 67, 2544, doi: 10.1016/j.asr.2021.01.042

Alipour, N., Mohammadi, F., & Safari, H. 2019, ApJS, 243, 20, doi: 10.3847/1538-4365/ab289b

Asaly, S., Gottlieb, L.-A., & Reuveni, Y. 2021, IEEE Journal of Selected Topics in Applied Earth Observations and Remote Sensing, 14, 1469, doi: 10.1109/JSTARS.2020.3044470

Barnes, G., Leka, K. D., Schrijver, C. J., et al. 2016, ApJ, 829, 89, doi: 10.3847/0004-637X/829/2/89

Brown, J. C. 1971, SoPh, 18, 489, doi: 10.1007/BF00149070

Chen, Y., Manchester, W. B., Hero, A. O., et al. 2019, Space Weather, 17, 1404, doi: 10.1029/2019SW002214

Deshmukh, V., Berger, T. E., Bradley, E., & Meiss, J. D. 2020, Journal of Space Weather and Space Climate, 10, 13, doi: 10.1051/swsc/2020014

Domijan, K., Bloomfield, D. S., & Pitié, F. 2019, SoPh, 294, 6, doi: 10.1007/s11207-018-1392-4

Fulbright, J. P., Kline, E., Pogorzala, D. R., et al. 2017, in Society of Photo-Optical Instrumentation Engineers (SPIE) Conference Series, Vol. 10402, Earth Observing Systems XXII, ed. J. J. Butler, X. J. Xiong, & X. Gu, 104020T, doi: 10.1117/12.2274358

Goodman, M. L., Kwan, C., Ayhan, B., & Shang, E. L. 2020, Frontiers of Physics, 15, 34601, doi: 10.1007/s11467-020-0956-6

Guerra, J. A., Murray, S. A., Shaun Bloomfield, D., & Gallagher, P. T. 2020, Journal of Space Weather and Space Climate, 10, 38, doi: 10.1051/swsc/2020042

Hanser, F. A., & Sellers, F. B. 1996, in Society of Photo-Optical Instrumentation Engineers (SPIE) Conference Series, Vol. 2812, GOES-8 and Beyond, ed. E. R. Washwell, 344–352, doi: 10.1117/12.254082

Huang, X., Wang, H., Xu, L., et al. 2018, ApJ, 856, 7, doi: 10.3847/1538-4357/aaae00

Jiao, Z., Sun, H., Wang, X., et al. 2020, Space Weather, 18, e02440, doi: 10.1029/2020SW002440

Leka, K. D., Park, S.-H., Kusano, K., et al. 2019, ApJS, 243, 36, doi: 10.3847/1538-4365/ab2e12

Li, X., Zheng, Y., Wang, X., & Wang, L. 2020, ApJ, 891, 10, doi: 10.3847/1538-4357/ab6d04

Liu, H., Liu, C., Wang, J. T. L., & Wang, H. 2019, ApJ, 877, 121, doi: 10.3847/1538-4357/ab1b3c

Lu, E. T., & Hamilton, R. J. 1991, ApJL, 380, L89, doi: 10.1086/186180

Morales, L. F., & Santos, N. A. 2020, SoPh, 295, 155, doi: 10.1007/s11207-020-01713-0

Mrozek, T., Tomczak, M., & Gburek, S. 2007, A&A, 472, 945, doi: 10.1051/0004-6361:20077652

Nishizuka, N., Kubo, Y., Sugiura, K., Den, M., & Ishii, M. 2021, Earth, Planets, and Space, 73, 64, doi: 10.1186/s40623-021-01381-9

Panos, B., & Kleint, L. 2020, ApJ, 891, 17, doi: 10.3847/1538-4357/ab700b

Park, E., Moon, Y.-J., Shin, S., et al. 2018, ApJ, 869, 91, doi: 10.3847/1538-4357/aaed40

Reeves, K. K., & Golub, L. 2011, ApJL, 727, L52, doi: 10.1088/2041-8205/727/2/L52

Ryan, D. F., Dominique, M., Seaton, D., Stegen, K., & White, A. 2016, A&A, 592, A133, doi: 10.1051/0004-6361/201628130

Savage, S. L., Holman, G., Reeves, K. K., et al. 2012, ApJ, 754, 13, doi: 10.1088/0004-637X/754/1/13

Shramko, A. D., Tlatov, A. G., & Guseva, S. A. 2019, Astronomical and Astrophysical Transactions, 31, 103

Su, Y. N., Golub, L., van Ballegooijen, A. A., & Gros, M. 2006, SoPh, 236, 325, doi: 10.1007/s11207-006-0039-z

Tadikonda, S. K., Freesland, D. C., Minor, R. R., et al. 2019, SoPh, 294, 28, doi: 10.1007/s11207-019-1411-0

Tlatov, A. G., Illarionov, E. A., Berezin, I. A., & Shramko, A. D. 2020, Cosmic Research, 58, 444, doi: 10.1134/S0010952520060106

Tobiska, W. K., Woods, T., Eparvier, F., et al. 2000, Journal of Atmospheric and Solar-Terrestrial Physics, 62, 1233, doi: 10.1016/S1364-6826(00)00070-5

Wang, J., Zhang, Y., Hess Webber, S. A., et al. 2020, ApJ, 892, 140, doi: 10.3847/1538-4357/ab7b6c

Zheng, Y., Li, X., & Wang, X. 2019, ApJ, 885, 73, doi: 10.3847/1538-4357/ab46bd